



1 Constructing physical-based rainfall landslides prediction model: 2 Insights from rainfall threshold curves database of slope units

3 Kai Wang^{1*}, Linmao Xie¹, Shuailong Xie¹, Shaojie Zhang^{2*}, Yongyang Jiang³, Ji Zhang⁴, Lin Zhu¹, Zhiliu Wang¹,
 4 Fuzhou Qi¹

5 *1. School of architecture and civil engineering, Zhongyuan University of Technology, Zhengzhou, 450007, China*

6 *2. Key Laboratory of Mountain Hazards and Earth Surface Process, Institute of Mountain Hazards and Environment,
 7 Chinese Academy of Sciences, Chengdu, 610041, China*

8 *3. Zhejiang Zhongnan Construction Group Steel Structure Co., Ltd, Hangzhou, 311400, China*

9 *4. Sichuan Institution of Geological Engineering Investigation Group Co.LTD, Chengdu, 610041, China*

10 **Abstract:** The commonly used rainfall threshold warning method relies heavily on historical
 11 rainfall and landslide inventory data, which limits its applicability in regions that lack these data.
 12 While physical methods do not rely on landslide inventories to establish warning criteria, the
 13 calculation of the safety factor typically requires considerable time. To address these issues, this
 14 study integrates physical methods, rainfall threshold warning methods, and slope units to develop a
 15 rapid forecasting model for rainfall landslides at a regional scale. A hydrological analysis technique
 16 for slope units based on grid cells was developed to calculate the instability probability of slope
 17 units. Then, each slope unit was analyzed under 20 levels of antecedent effective precipitation and
 18 nearly 200 combinations of rainfall intensity (I) and duration (D) to derive the key fitting parameters
 19 α and β of the I-D curves under various rainfall scenarios. The application results from Fengjie
 20 County indicate that the model runs in less than 12 min, with missing alarm and false alarm rates of
 21 11.8% and 21.1%, respectively, highlighting its excellent potential for practical application. This
 22 study is expected to provide insights for the rapid forecasting of rainfall landslides in the
 23 impoverished mountainous regions of developing countries.

24
 25
 26 **Key words:** Landslide forecasting model, Slope unit, Fitting parameters, Warning database

27
 28
 29
 30
 31
 32
 33

* Corresponding Authors 1: Kai Wang
 E-mail: 6696@zut.edu.cn

* Corresponding Authors 2: Shaojie Zhang
 E-mail: sj-zhang@imde.ac.cn



1 Introduction

Rainfall-induced landslides at a regional scale are among the most common types of natural hazards worldwide. Reports indicate that in the United States, rainfall-triggered landslides and secondary hazards result in 25–50 fatalities and economic losses of approximately \$2 billion annually (He et al., 2016). This loss is even more severe in developing countries in the Third World (Wang et al., 2024; Wang et al., 2021; Wang et al., 2023). In recent years, numerous studies have indicated that regional landslide forecasting is highly effective for hazard prevention and mitigation. Researchers have developed various rainfall landslide forecasting models based on statistical and physical methods (Aristizábal et al., 2016; Baum et al., 2008; Bezak et al., 2016; Bogaard et al., 2018; Cuomo et al., 2021; Liang et al., 2021; Medina et al., 2021; Pinho et al., 2022; Tufano et al., 2021; Wang et al., 2013; Zhang et al., 2021; Zhang et al., 2019). However, there are still several unresolved issues in regional landslide forecasting, making accurate and efficient warnings a significant global challenge.

The first major issue is the selection of forecasting methods. The presented statistical approaches generally depend on historical precipitation and landslide inventory data to construct the rainfall threshold curves. Recently, researchers proposed different types of rainfall threshold curves, including I-D, E-D, E-I, IR-AER, I-P, and I-D-MEAR (Brunetti et al., 2010; Hong et al., 2005; Rosi et al., 2020; Zhuang et al., 2014). The I-D curve is the most extensively used among these types. The I-D curve is typically fitted in either Cartesian coordinates or a double-logarithmic coordinate system, and the equation of the curve is governed by two key fitting parameters, α and β , expressed as follows:

$$I = \alpha D^{\beta} \quad (1)$$

where α and β are derived from the statistical analysis of historical rainfall and landslide data.

Studies indicate that statistical methods are applicable in regions with abundant historical records of rainfall landslides because these areas can provide sufficient samples for fitting the I-D curve (Bezak et al., 2016; Hong et al., 2017; Kanungo et al., 2014; Kim et al., 2020; Ma et al., 2015; Marra, 2018; Pradhan et al., 2018). However, in the poor mountainous regions of the Third World, many areas that are severely affected by landslides lack professional monitoring devices and rain gauges, potentially limiting the application of statistical approaches (Zhang et al., 2021; Zhang et al., 2019). In contrast, physical methods typically rely on hydrological and mechanical analyses to



1 calculate the safety factors of landslides under different rainfall scenarios, thereby reducing the
2 reliance on historical rainfall and landslide observation data. In regions where landslide inventory
3 data are scarce, physical methods could serve as promising alternatives (Zhang et al., 2021; Zhang
4 et al., 2019). However, physical methods require historical landslide data to validate the accuracy
5 of the forecasting results, and the safety factor calculation process typically requires a considerable
6 amount of time. This computational burden increases substantially when considering the stability
7 analysis of thousands of slopes at the regional scale, making it difficult to ensure the efficiency of
8 real-time warnings (Zhang et al., 2021).

9 The second issue pertains to the selection of prediction unit. Clearly defined prediction units
10 enable residents to identify the specific locations where landslides are likely to occur while also
11 providing guidance for local governments to develop emergency schemes. However, the I-D
12 warning curves derived from statistical methods can only provide general trends of hazards within
13 the region but cannot pinpoint the specific locations of landslide occurrences. Grid cells improve
14 the clarity of the prediction results to some extent, as the specific locations of each grid within the
15 area are well defined (Zhang et al., 2021). Researchers have employed grid cells to establish multiple
16 physical forecasting models such as SHALSTAB (Montgomery et al., 1994), SINMAP (Tarboton et
17 al., 1970), GEOTOP-FS (Rigon et al., 2006), Trigrs (Baum et al., 2008), HIRESSS (Rossi et al., 2013),
18 H-slider (Liang et al., 2021), SHIA_Landslide (Aristizábal et al., 2016), SLIP (Montrasio et al., 2016),
19 and FSLAM (Guo et al., 2022). However, the morphology of grid cells does not accurately
20 characterize the topographical features of natural hillslopes (Domènech et al., 2019; Zhang et al.,
21 2021), resulting in a lack of clear geomorphological significance. In practical applications, a natural
22 slope can be segmented into a series of grid cells, in which each grid is assigned a different alert
23 level. This indicates that a high warning level in a grid cell does not mean that the entire slope will
24 experience a slide.

25 In contrast, slope units can represent the topographical features of landslides more accurately,
26 and their boundaries are easily discernible in field environments. Currently, there are various
27 methods for extracting slope units, including the DEM-based hydrological process analysis
28 method (Turel et al., 2011), r.slopeunits method (Alvioli et al., 2020), curvature watershed
29 methods (Yan et al., 2021), MIA-HSU methods (Wang et al., 2019), and multi-scale image
30 segmentation methods (Huang et al., 2021). In recent years, researchers have developed forecasting



1 models utilizing slope units, validating their promising application potential in predicting rainfall-
2 induced landslides (Wang et al., 2023; Zhang et al., 2021).

3 Addressing the issues outlined in regional landslide forecasting, this study focuses on the
4 integration of slope units, physical methods, and rainfall parameterized warning techniques to
5 develop a rapid forecasting model applicable to large areas on a scale of thousands of square
6 kilometers. Within this model, we no longer pay attention to the positional relationship between the
7 rainfall data of a landslide and the I-D curve, but concentrate on the key fitting parameters α and β
8 of the I-D curve for each slope unit. To facilitate this, we developed a rainfall infiltration simulation
9 technique rooted in grid cells within slope units and subsequently utilized physical methods to
10 analyze the instability probability for slope units under different rainfall scenarios. For each slope
11 unit, we designed rainfall scenarios comprising various antecedent rainfall levels combined with
12 hundreds of rainfall intensity and duration combinations. This allowed us to obtain the key
13 parameters α and β of the I-D curves for different rainfall scenarios, thereby constructing a database
14 of parameters α and β under various antecedent precipitation levels. A case study in Fengjie County,
15 in the Three Gorges Reservoir area, was conducted to validate the reliability of the proposed method.
16 This research is expected to provide valuable insights for regional landslide forecasting in
17 impoverished mountainous areas in the developing world.

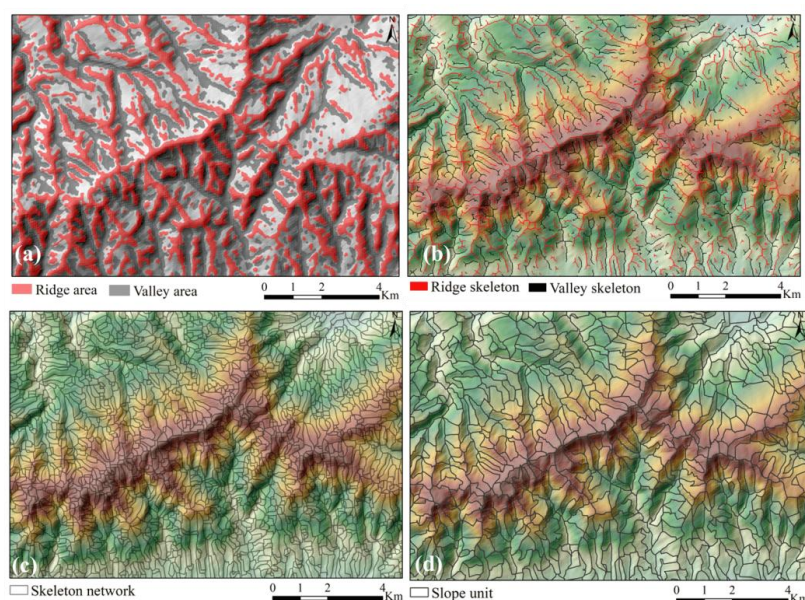
18 **2 Methodology**

19 **2.1 The slope unit extraction method MIA-HSU**

20 In this study, we employed the MIA-HSU method to extract slope units(Wang et al., 2021;
21 Wang et al., 2019; Wang et al., 2023). In the MIA-HSU method, each HSU(homogeneous slope unit)
22 is defined as a continuous and homogeneous geomorphological entity. This definition implies that
23 terrain features related to slope and aspect are uniform within each HSU, with boundaries indicating
24 transitions in topographical features. The MIA-HSU method consists of two steps. The first step
25 involves partitioning the Digital Elevation Model (DEM) into small regions with homogeneous
26 terrain characteristics. In this step, the MIA-HSU method utilizes terrain curvature analysis to
27 identify ridge and valley regions (Figure 1a) and then extracts the morphological skeleton lines of
28 ridge and valley areas to characterize topographic relief. Morphological algorithms (such as dilation
29 and erosion) were used to extract the morphological skeletons of ridges, valleys, and flat areas from
30 the DEM (Figure 1b), ultimately connecting these skeletons into a closed network (Figure 1c). Thus,



1 each small region within the network exhibits uniform geomorphological characteristics. The
 2 second step involves merging small adjacent regions. The MIA-HSU method employs the principal
 3 component analysis (PCA) method to derive fitted planes from localized terrain regions, followed
 4 by the implementation of vector similarity criteria to merge adjacent small regions, thereby
 5 generating HSUs(Figure 1d).



6
 7 Figure 1 HSU extraction process: a. the identification of ridge and valley areas; b. the morphological skeleton line
 8 extraction for ridge and valley areas; c. the morphological skeleton closed network; d. HSU extraction result

9 **2.2 The HSU hydrologic simulation technique based on grid cells**

10 **(1) The identification for row and column information of grid cell within HSUs**

11 From a geometric perspective, an HSU can be regarded as a spatial polygon that signifies a
 12 landform entity with homogeneous terrain features in the field environment. At the regional scale,
 13 there is obvious heterogeneity in the topography and boundary characteristics among different
 14 HSUs(Wang et al., 2021; Wang et al., 2019; Wang et al., 2023), resulting in the immaturity of
 15 hydrological analysis methods based on slope units. In contrast, hydrological analysis methods
 16 based on grid cells are well-developed. Some researchers have employed grid cells integrated with
 17 an infinite slope model or the limit equilibrium method to conduct regional landslide assessment or
 18 prediction(Gu et al., 2014; Wang et al., 2023; Zhang et al., 2021; Zhuang et al., 2016). In this study,
 19 each HSU was conceptualized as a composition of grid cells with similar microtopographic features,
 20 as illustrated in Figure 2a. For each HSU, we utilized GIS spatial analysis tools to quantify the

(a)

(b)

(2) Initial water content assignment of HSUs

In this study, each grid cell is stratified into ten soil layers, each with a thickness of 0.2 m (Figure 2b). For the Three Gorges Reservoir area, the regional landslides triggered by rainfall were mainly shallow (with thicknesses of 2-3 m). Therefore, variations in residual moisture content within the soil depth were disregarded, and the same residual moisture content value was assigned to each soil layer. Following this, we applied steady-state infiltration theory to simulate the



1 distribution of moisture content across the soil layers influenced by antecedent precipitation, thereby
 2 allocating the antecedent rainfall to each soil layer. The calculation for θ_{ini} of each soil layer within
 3 the grid cell is as follows:

$$4 \quad \theta_{ini}(k) = \theta_{ante}(k) + \theta_{res} \quad (k=1,2,3 \dots n) \quad (2)$$

5 Where n represents the number of soil layers, and here $n = 10$; $\theta_{ini}(k)$ indicates the initial
 6 moisture content of each soil layer; $\theta_{ante}(k)$ refers to the moisture change in each soil layer due to
 7 previous precipitation; θ_{res} stands for the residual moisture content in the grid cell.

8 (3) Rainfall infiltration process simulation of grid cell

9 After obtaining the initial moisture content distribution, the 1-dimensional Richards infiltration
 10 equation was used to solve the moisture content distribution in the grid cell during the rainfall
 11 infiltration process.

$$12 \quad \frac{\partial \theta}{\partial t} = \frac{\partial}{\partial z} \left[D(\theta) \cdot \frac{\partial \theta}{\partial z} \right] - \frac{\partial K(\theta)}{\partial z} \quad (3)$$

13 Where $D(\theta)$ represents the value of soil water diffusivity under unsaturated conditions and has

$$14 \quad D(\theta) = K(\theta) / \frac{d\theta}{d\psi_m} .$$

15 The finite difference scheme outlined above was formulated for numerical simulation of
 16 hydrological processes. The lower boundary, identified as impermeable, is based on the maximum
 17 soil depth of the grid cell. The upper boundary of each grid cell was designated as an infiltration
 18 boundary. When the rainfall intensity $I(t)$ is less than the infiltration capacity of the topsoil, all
 19 precipitation infiltrates into the soil, and no runoff is generated. In this scenario, the infiltration
 20 boundary of precipitation was governed by the following differential equation:

$$21 \quad -D(\theta) \frac{\partial \theta}{\partial z} + K(\theta) = I(t) \quad (4)$$

22 When the rainfall intensity exceeded the soil infiltration capacity, the excess portion was
 23 transformed into overland flow. At this point, the rainfall infiltration boundary was governed by the
 24 following equation:

$$25 \quad \theta = \theta_s \quad (5)$$

26 Where θ_s is the saturated water content of the grid cell.

27 (4) Soil water content generation of HSU

28 Following the calculation of the soil moisture for individual grid cells, the soil water
 29 distribution of the HSU was computed as follows:



$$\theta_{HSU}(k) = \frac{\sum_{k=1}^n \theta(k)}{n} \quad (6)$$

where $\theta_{HSU}(k)$ represents the moisture content of the k th layer of the HSU, $\theta(k)$ denotes the moisture content of the k th layer in the grid cell. n is the number of soil layers ($n = 10$).

2.3 HSU_{prob}: the calculation of instability probability of HSUs

(1) Profile extraction

After calculating the soil water content within each HSU, analyzing the stability of HSUs during the rainfall infiltration process is another important task. At present, the time required to carry out 3D analysis for each HSU on a large regional scale is too large, so extracting the calculation profile of the HSU becomes a reasonable selection. Currently, there is no uniform method for extracting the calculation profile of HSUs. Some reasonable assumptions are summarized as follows: the position of the profile line should reflect the elevation difference between the front and back edges of the slope, and the centroid point of the HSUs should be on the calculated profile to ensure that the soil weight on both sides of the calculated section is relatively uniform, and the areas of the two sections should be close to each other.

Based on these considerations, we developed a fast extraction algorithm HSU-profil (Wang et al., 2021; Wang et al., 2023) for HSU profiles at large regional scales, which can be divided into three steps:

First, the highest elevation point H of the HSU polygon is connected to centroid point C to obtain line segment L_1 , which intersects the HSU polygon at point J_1 (Figure 3b). Line segment L_1 divides the HSU polygon into two parts, and the areas of the two parts, S_1 and S_2 are calculated to obtain the area ratio $A = S_1 / S_2$.

Next, the lowest elevation point L and centroid C are connected to form line segment L_2 , as shown in Figure 3 b. Determine the intersection point J_2 between L_2 and the polygon of the slope unit is determined. At this point, the HSU was divided into two parts by line segment L_2 , and the areas of the two parts, S_3 and S_4 , were calculated to obtain the area ratio $B = S_3 / S_4$.

Finally, $|A|$ and $|B|$ are compared. A smaller absolute value of A indicates that line segment L_1 divides the areas on both sides of the HSU polygon more evenly. In this case, L_1 is selected as the profile line. Otherwise, the line segment L_2 was chosen as the profile line.

(2) Calculation of safety factor F_s calculation



For each HSU, the Monte Carlo method was used to generate a large number of potential
 polyline-type slip surfaces (Figure 3c), and the random walk method (Greco, 1996) was employed
 to search for the critical slip surface. The infinite slope model was used to calculate the safety factor
 F_s of each potential slip surface as follows:

$$F_s = \frac{\tan \varphi}{\tan \alpha} + \frac{c + u_s \tan(\varphi^b)}{\gamma_s D_s \cos \alpha \sin \alpha} \quad (7)$$

where c is the effective cohesion of the soil, φ is the effective internal friction angle of the soil,
 and γ_s is the average unit weight of soil above the slip surface. φ^b is related to the matric suction;
 when the matric suction is low, it is close to the internal friction angle (Zhang et al., 2018). D_s is the
 thickness of the soil layer above the slip surface. u_s represent the matric suction, which can be
 described by the Van Genuchten model (Van Genuchten, 1980):

$$S_e = \frac{\theta - \theta_r}{\theta_s - \theta_r} = \left[\frac{1}{1 + (\alpha_w \times u_s)^n} \right]^m \quad (8)$$

Where S_e represents the saturation degree, θ denotes the soil water content of the HSU, θ_s and θ_r are
 the saturated and residual water content, respectively. The parameters α_w , n and m characterize the
 shape of the soil–water characteristic curve, with the relationship $n=1-1/m$.

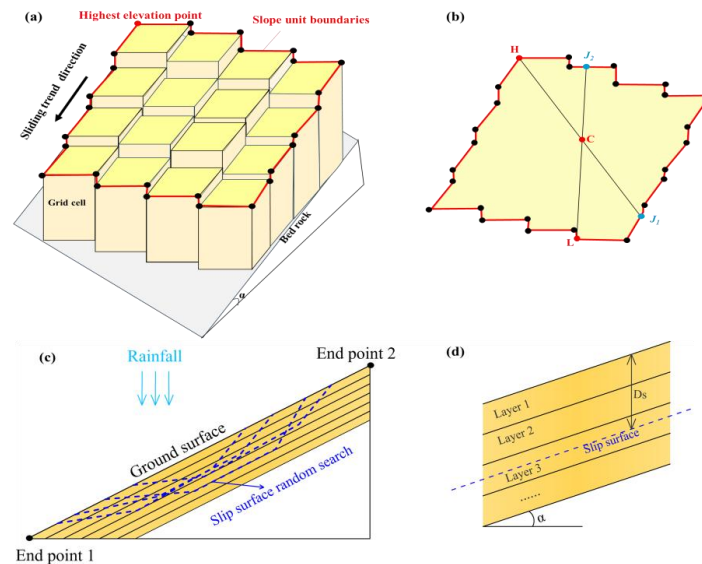


Figure 3 HSU instability probability calculation diagram a. Extraction of HSU boundary points; b. Profile line
 extraction of HSU polygon; c. Random search for critical slip surface; d. Enlarged view of the sliding mass for
 detailed visualization.



(3) HSU_{prob} calculation

According to the saturated-unsaturated rainfall infiltration theory, the mechanical parameters of the soil (such as cohesion force $c(kPa)$ and internal friction angle $\varphi(^{\circ})$) are significantly affected by soil moisture content fluctuations. The variation in soil mechanical parameters during the process of rainfall infiltration is very complex, and it is generally acknowledged that dry soil prior to rainfall infiltration exhibits higher mechanical strength (characterized by elevated parameter values). As rainwater continues to infiltrate, the soil water content gradually increases, leading to a decreasing trend in mechanical parameters, such as cohesion and internal friction angle. Consequently, the mechanical parameters of the soil within each HSU are not fixed, but spatial uncertainty exists to some extent. In this context, employing probabilistic analysis methods to calculate the instability probability of an HSU is a more reasonable choice. Probability density functions (such as normal or uniform distributions) are commonly used to describe the uncertainty of the geotechnical parameters. The normal distribution is considered suitable for small areas or watersheds where hydrogeological parameters can be collected in detail, whereas a uniform distribution is more applicable for larger areas, where it is difficult to acquire detailed hydromechanical parameters (Wang et al., 2021; Wang et al., 2023).

In this study, we utilized a uniform distribution to simulate the uncertainty of the mechanical parameters within the HSUs. The soil mechanical parameters in the unsaturated state before rainfall were taken as the upper bound, while those in the fully saturated state were considered the lower bound, thereby establishing the upper and lower value boundaries for the mechanical parameters within the HSU, as indicated in Equations (9) and (10):

$$c \in [c_{lower}, c_{upper}] \quad (9)$$

$$\varphi \in [\varphi_{lower}, \varphi_{upper}] \quad (10)$$

where c_{upper} and c_{lower} represent the upper and lower bounds of $c(kPa)$, respectively, φ_{upper} and φ_{lower} represent the upper and lower bounds of $\varphi(^{\circ})$, respectively. The Monte Carlo method was employed to randomly select the values within these bounds. The instability probability of the HSU was calculated using Equation (11).

$$HSU_{prob} = \frac{Sum_{Fs < 1}}{m} \quad (11)$$

where m represents the number of random selections for the mechanical parameters and m



1 is set to 500.

2 **2.4 The obtainment of key fitting parameters α and β for I-D curves of HSUs**

3 In this study, an HSU is regarded as unstable when the value of HSU_{prob} exceeds 50%. Then,
 4 the rainfall intensity and duration data with HSU instability under different rainfall scenarios were
 5 recorded to obtain the key fitting parameters α and β for the I-D curves of each HSU, thereby
 6 establishing a database of parameters α and β . The detailed steps are as follows.

7 (1) Setting the antecedent effective rainfall levels $AER_i (i=1,2,3 \dots n)$

8 The antecedent effective rainfall(AER) has a significant impact on landslide occurrence.
 9 Previous research indicates that in the Three Gorges Reservoir area, the minimum value of AER
 10 before landslide occurrence is 0 mm, whereas the maximum value of AER can exceed 170
 11 mm(Wang et al., 2021). Therefore, 20 different levels of AER ranging from 0 to 200 mm were
 12 established with intervals of 10 mm.

13 (2) Design of the combination of rainfall intensity (I) and duration(D)

14 For each antecedent rainfall level, we categorized rainfall intensity (I) into eight levels to
 15 represent the variation from light to heavy rainstorms: 2, 5, 10, 20, 30, 40, 50, and 60 mm/h. The
 16 rainfall duration (D) ranged from 1 to 24 h, with intervals of one hour. Consequently, 192
 17 combinations of I and D were generated for each AER level.

18 (3) Generation of fitting parameters α , β of the I-D curves

19 For each combination of rainfall intensity and duration data, the method outlined in Section
 20 2.2 is used to determine the soil water distribution within each HSU, and the corresponding value
 21 of HSU_{prob} was computed using the method described in Section 2.3. If the HSU is unstable, the
 22 corresponding intensity and duration data can serve as data points for fitting the I-D curves.
 23 Subsequently, a power function was utilized to fit these data points to obtain the key fitting
 24 parameters α and β of the I-D curve. As presented above, the fitting parameters α and β for the I-D
 25 curve of each HSU can be generated, thereby establishing a database for α and β at different AER
 26 levels.

27 **2.5 Warning Mode**

28 In practical applications, the antecedent effective rainfall(AER), rainfall intensity (I), and
 29 duration (D) for each HSU can be computed using Quantitative Precipitation Estimation (QPE) and
 30 Quantitative Precipitation Forecasting (QPF) products provided by the meteorological department



(Wang et al., 2021). Next, we analyzed the relationship between the actual value of AER and the 20 levels of AER documented in the database, thereby determining the level that is closest to the antecedent effective rainfall data of the HSU. The α and β values corresponding to this level were retrieved from the database for the following assessments.

(1) If $I \geq aD^\beta$, the data point (I, D) is above the warning curve; thus, the warning should be released.

(2) Conversely, if $I < aD^\beta$, it signifies that the data point (I, D) is below the warning curve; therefore, no warning should be issued.

The programming languages Fortran 95 and Python 3.1 were employed to compile the algorithms outlined in Sections 2.1-2.5, and the overall flowchart of the warning mode is depicted in Figure 4.

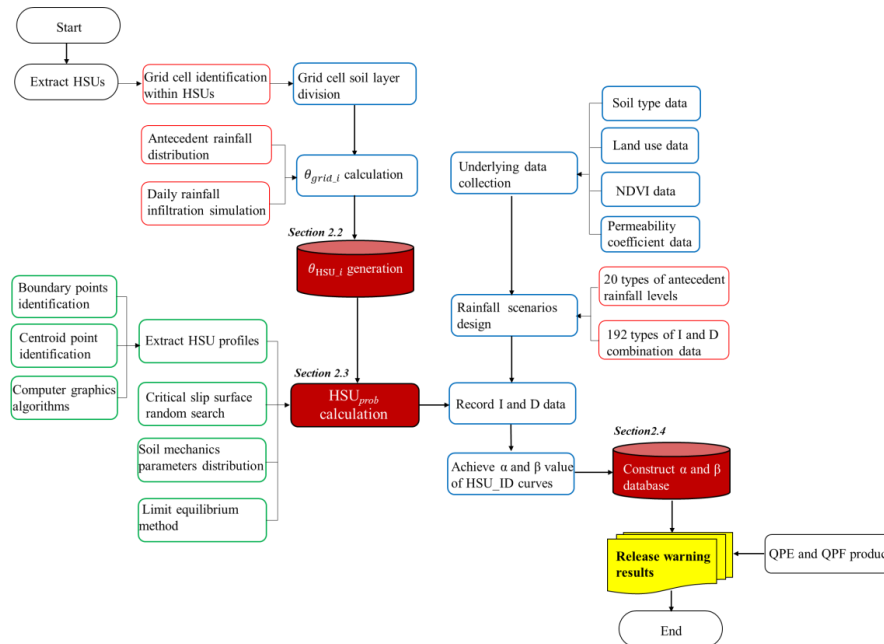


Figure 4 The flow chart of the fast warning mode based on parameter α and β database

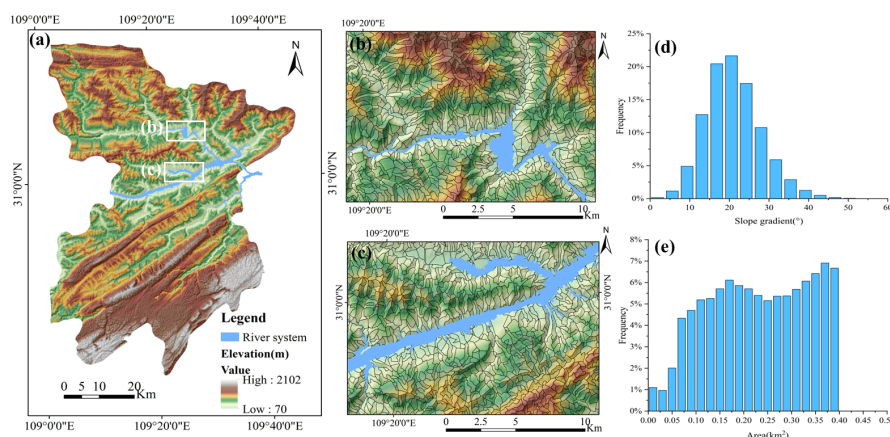
3 Study area and data

3.1 Study area and slope unit data

Fengjie County is situated in the eastern region of the Three Gorges Reservoir area, with geographical coordinates ranging from 109°1'17" " to 109°45'58" East and 30°29'19" to 31°22'33" North, covering a total area of 4087 km². The region has a subtropical humid monsoon climate with



1 an annual average rainfall of 1,500–2,000 mm. The rainy season occurs from May to September,
 2 accounting for 70% of the annual precipitation. The terrain is primarily mountainous and the
 3 Yangtze River flows across the region from west to east. Geological hazards, such as landslides,
 4 debris flows, and collapses, are widely distributed in Fengjie County, with rainfall landslides posing
 5 the most significant threat. Based on the 7m DEM of Fengjie (Figure 5a), the MIA-HSU method
 6 was employed to extract the slope units, resulting in the identification of 17,547 HSUs(Figures 5 b
 7 and c). Histograms of the slope gradient and area distribution of the HSUs are presented in Figure
 8 5d-e. As shown in Figure 5d, the slope gradients of the HSUs follow a normal distribution, with
 9 85.4% of the slopes falling within the range of 10° to 30°. Figure 5e illustrates that the average
 10 area of the HSUs is 0.23 km², with 53.9% of the slope units having an area less than 0.25 km².
 11 Because the sliding depth of shallow landslides typically ranges from 2 m to 3 m, the majority of
 12 HSUs can be classified as small-to medium-scale landslides (with volumes under 500,000 m³).



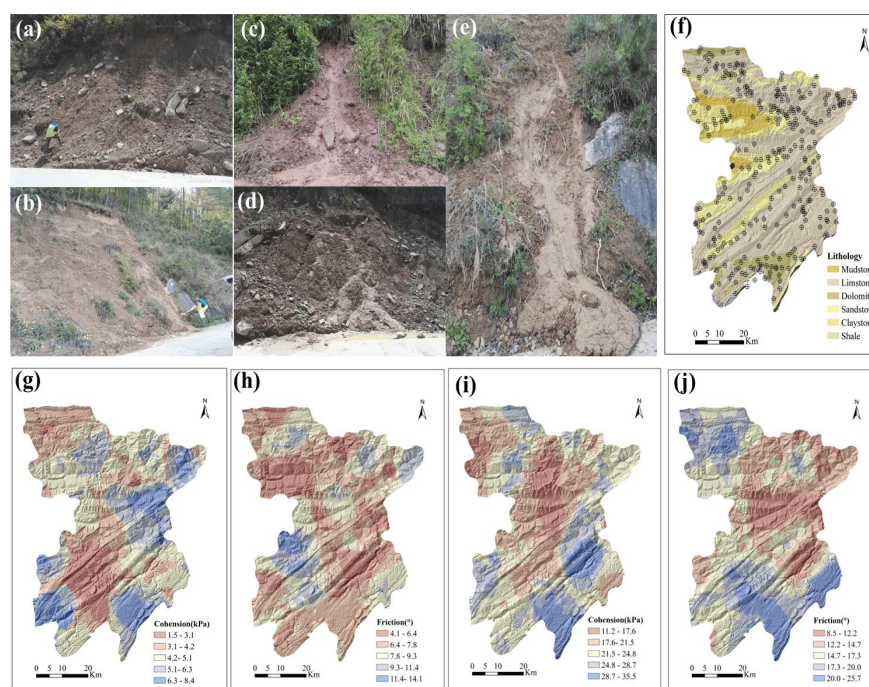
13
 14 Figure 5 Division of HSUs in Fengjie County a. Fengjie DEM; b and c. Extraction results for selected regions:
 15 Enlarged View; d. Histogram of slope distribution of HSUs; e. Histogram of area distribution of HSUs.

16 3.2 Soil mechanical parameter c (kPa) and ϕ (°) data of HSUs

17 The rainfall-triggered shallow landslides within the study area are mainly composed of
 18 quaternary clay and silt, which are classified as fine-grained soils(Wang et al., 2021; Wang et al.,
 19 2023). Field investigations indicate that the sliding soil is fully or even oversaturated, with some
 20 soil mass transitioning into mudflow during the sliding process. The laboratory moisture content
 21 tests revealed that the soil water content under these conditions approached or exceeded the liquid
 22 limit. To obtain detailed soil mechanical parameters under different moisture states, we conducted



1 extensive field sampling across Fengjie County, resulting in 312 sampling points, as depicted in
 2 Figure 6f. For each sampling point, direct laboratory shear tests were performed to derive the soil
 3 mechanical parameters c (kPa) and ϕ ($^{\circ}$) at the liquid and plastic limits, respectively. Subsequently,
 4 ArcGIS spatial analysis tools were utilized to generate distribution maps of c (kPa) and ϕ ($^{\circ}$) under
 5 plastic and liquid limit moisture conditions, as shown in Figures 6g-j.



6
 7 Figure 6 State of Landslide Soil Before and After Rainfall (a. Soil approaching plastic limit moisture content before
 8 rainfall; b. Soil approaching plastic limit moisture content before rainfall; c. Soil in a fluid state after rainfall; d. Soil
 9 in a fluid state after rainfall; e. Fully saturated and liquefied soil after rainfall; f. Soil sampling locations; g. c (kPa)
 10 at plastic limit moisture content; h. ϕ ($^{\circ}$) at plastic limit moisture content; i. c (kPa) at liquid limit moisture content;
 11 j. ϕ ($^{\circ}$) at liquid limit moisture content.)

12 3.3 Rainfall data

13 Rainfall data sources include Quantitative Precipitation Forecasting (QPF) products and
 14 Quantitative Precipitation Estimation (QPE) products. The QPF product obtained from the local
 15 government of Fengjie County is typically utilized to forecast future rainfall at a regional scale,
 16 which can provide rainfall forecast products for the next hour. QPE data are applied to estimate
 17 historical regional rainfall at a regional scale and are essential for determining the antecedent
 18 effective rainfall (AER), which can be computed as follows:



$$AER = \sum_{i=1}^n a^n R_i \quad (12)$$

Where AER is the antecedent effective rainfall, a is the attenuation coefficient, which is equal to 0.84, based on the research of the Fengjie count (Wang et al., 2021), n is the number of days before the landslide occurs.

4 Case Study: Rainfall-induced landslides of 31 August, 2014

From August 30–31, 2014, Fengjie experienced continuous heavy rainfall, triggering a series of landslide hazards that resulted in over 30 fatalities and an economic loss of 580 million yuan. Based on the daily QPE data for August 15–31, the effective precipitation for the 15 days prior to the landslide hazards is shown in Figure 7. As illustrated in Figure 7, the maximum precipitation during this period was 179.10 mm, which occurred in the northwestern region of the area. The hourly QPF data for August 31 are presented in Figure 8 *a-l*. As illustrated in Figure 8 *a-d*, the rainfall was minimal from 00:00 to 08:00, with a maximum cumulative rainfall of 12.2 mm 08:00. As shown in Figures 8e-g, rainfall began to increase rapidly at 10:00, reaching a maximum cumulative precipitation of 92.40 mm by 14:00 in the northwestern region of Fengjie County. Figures 8 h-l indicate that from 16:00 to 24:00, the cumulative rainfall remained constant, suggesting that the rainfall process had ceased.

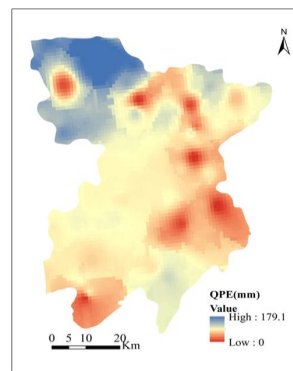
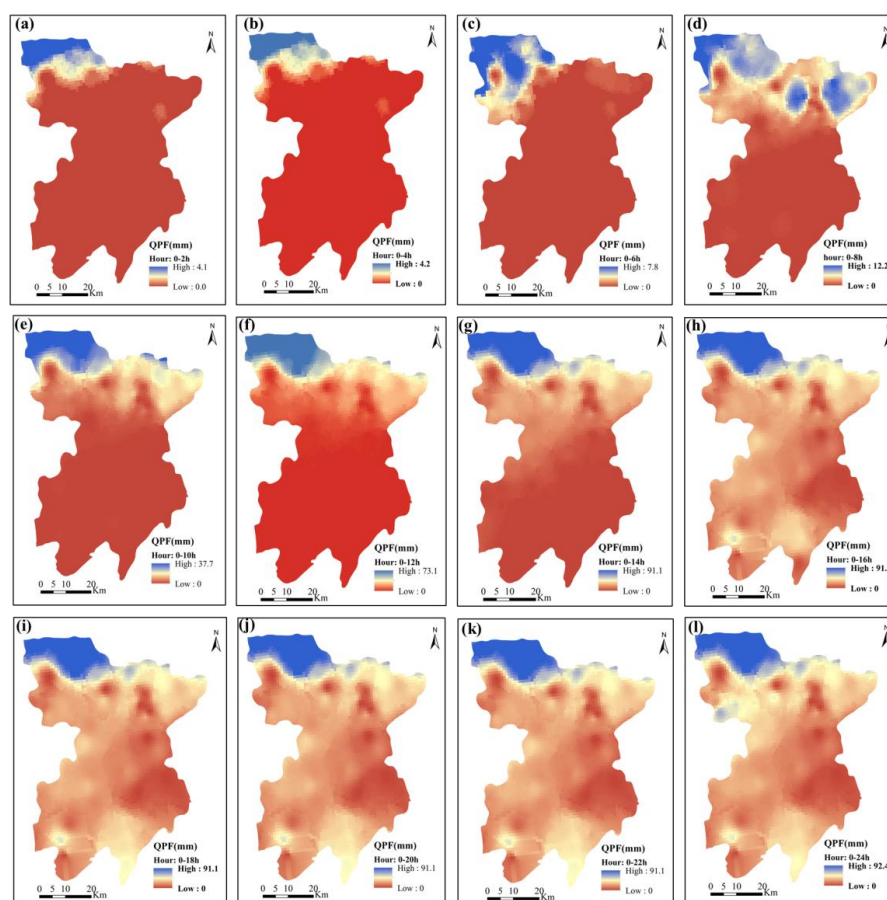


Figure 7 Precipitation Data Processing (Effective Precipitation from August 15 to August 30, 2014)



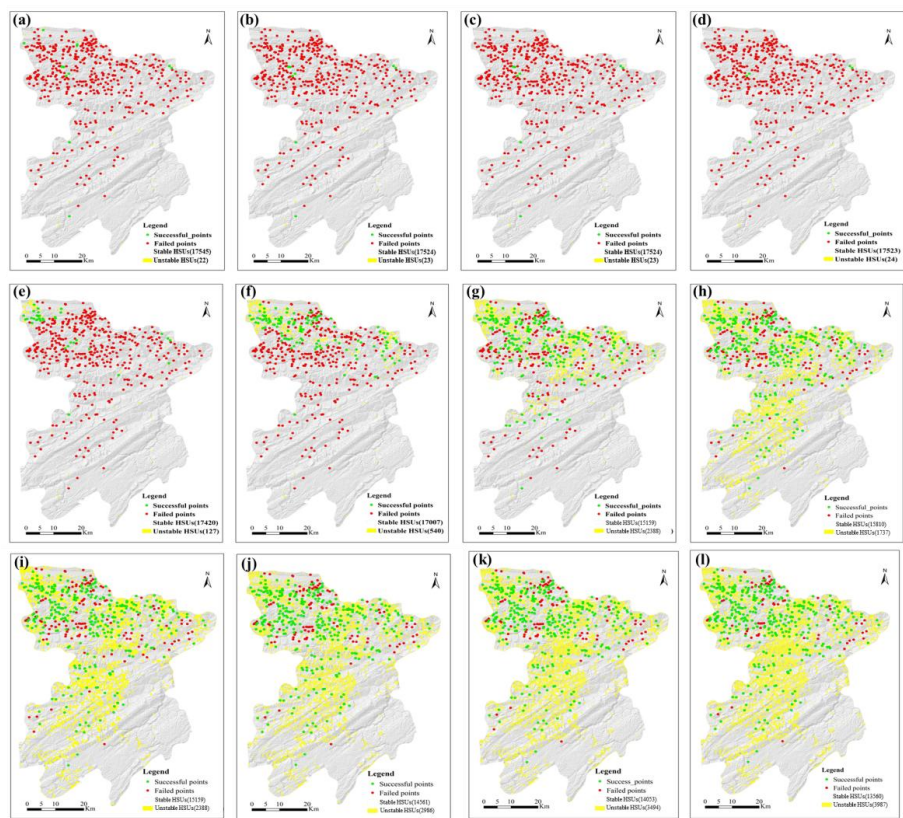
1
 2 Figure 8 Radar forecast precipitation data for 2014/08/31 (a. 2:00; b. 4:00; c. 6:00; d. 8:00; e. 10:00; f. 12:00; g.
 3 14:00; h. 16:00; i. 18:00; j. 20:00; k. 22:00; l. 24:00)

4 The Land and Resources Bureau of Fengjie County provided data on landslide points
 5 triggered by rainfall on August 31. This heavy precipitation triggered 583 landslides, which were
 6 mainly distributed in the northwestern region (as indicated by the red and green solid points in
 7 Figure 9). This study utilized the QPE (Figure 7) and QPF data (Figures 8 a-l) as inputs to forecast
 8 landslide hazards for August 31.

9 The landslide forecast results from 02:00 to 24:00 are shown in Figures 9(a-l). It can be seen
 10 from Figures 8 and 9 that there is a good correlation between the spatial distribution of unstable
 11 HSUs and rainfall characteristics. As presented in Figures 9a-d, at the beginning of the rainfall
 12 process (before 8:00), the majority of the HSUs remained stable owing to the minimal rainfall.
 13 Unstable HSUs began to emerge in the northwestern region starting at 10:00, coinciding with the



1 rapid increase in rainfall. Additionally, as the rainfall progressed, the number of unstable HSUs
2 increased swiftly and spread towards the central and southern regions (Figures 9f-g). Notably, many
3 unstable slope units appeared within several hours after heavy rainfall ceased. Figures 9h-l reveal
4 that from 16:00 to 24:00, although the heavy rainfall essentially ended, the number of unstable HSUs
5 continued to rise because of the moisture infiltration of the saturated top soil, reaching a total of
6 3,987 at 24:00.



7
8 Figure 9 Prediction results at 02:00 to 24:00 (a. 2:00; b. 4:00; c. 6:00; d. 8:00; e. 10:00; f. 12:00; g. 14:00; h. 16:00;
9 i. 18:00; j. 20:00; k. 22:00; l. 24:00)

10 This study employs the Receiver Operating Characteristic (ROC) method to analyze the
11 predictive performance of the HSU (Fawcett, 2006). For physically model-based slope units, the
12 ROC method describes the following four possible states using a contingency table:

- 13 ① True Positive (TP): HSU contain landslide points and exhibit instability;
14 ② True Negative (TN): HSU does not contain landslide points and does not exhibit instability;



③ False Positive (FP): HSU does not contain landslide points but exhibits instability;

④ False Negative (FN): HSU contains landslide points but does not exhibit instability.

According to GIS spatial statistics, 583 landslides triggered by rainfall on August 31 were contained within 425 HSUs. In this study, these HSUs are taken as benchmark values for the calculation of TP, TN, FP, and FN, and the missing alarm rate (MAR) and false alarm rate (FPR) can be calculated as follows:

$$\text{MAR} = 100\% \times \text{FN} / 425 \quad (13)$$

$$\text{FPR} = 100\% \times \text{FP} / (\text{FP} + \text{TN}) \quad (14)$$

The detailed forecast results for 02–24h are shown in Table 1. As shown in columns 7–8 of Table 1, with increasing rainfall duration, the Missing Alarm Rate (MAR) gradually decreases, while the False Positive Rate (FPR) gradually increases. Taking the result of 24h as an example, the MAR of 24h is 11.8% and the FPR is 21.1%, indicating that the prediction result can satisfy the requirement of early warning practice.

Table 1 Analysis of Forecast Results for the 831 Case Study

Forecasting hour(h)	Unstable HSUs	TP	TN	FP	FN	MAR (%)	FPR (%)
02	22	7	17097	25	418	98.4	0.1
04	23	3	17102	20	422	99.3	0.1
06	23	3	17102	20	422	99.3	0.1
08	24	2	17100	22	423	99.5	0.1
10	127	27	17022	100	398	93.6	0.6
12	540	116	16698	424	309	72.7	2.5
14	1370	231	15983	1139	194	45.6	6.7
16	1737	289	15674	1448	136	32.0	8.5
18	2388	327	15061	2061	98	23.1	12.0
20	2986	354	14490	2632	71	16.7	15.4
22	3494	364	13992	3130	61	14.4	18.3
24	3987	375	13510	3612	50	11.8	21.1

According to the ROC method, the precision and accuracy of the prediction results were calculated as follows:

$$\text{Precision} = \text{TPR} / (\text{TPR} + \text{FPR}) \quad (15)$$

$$\text{Accuracy} = (\text{TP} + \text{TN}) / (\text{TP} + \text{FN} + \text{TN} + \text{FP}) \quad (16)$$

Table 2 provide the calculation results of precision and accuracy at 24h. As shown, the precision of the forecasting results is 80.7%, with an accuracy value of 79.1%, indicating the proposed warning mode has satisfactory comprehensive forecasting performance.



Table 2 Calculation Results of Precision and Accuracy at the 24th Hour

Forecasting hour(h)	Unstable HSUs	TP	TN	FP	FN	Precision(%)	Accuracy(%)
24	3987	375	13510	3612	50	80.7	79.1

5 Discussion

5.1 The discussion on the computational efficiency

For emergency warnings during the rainy season, the swift release of warning information is crucial for local authorities to develop emergency plans and to evacuate residents from landslide-prone areas. Therefore, local governments not only seek satisfactory accuracy in the warning model but also require minimal time. To evaluate the computational efficiency of the proposed model, a standard laptop was utilized to execute the forecast for landslide hazards on August 31. The device specifications and computation times are presented in Table 3. As shown in Table 3, for the regional scale covering several thousand square kilometers, the prediction model can rapidly complete real-time warnings for the next 24 h within 12 min, indicating that its computational efficiency can satisfy the requirements of emergency warning.

Table 3 Analysis of computational efficiency of the prediction model

Area (m ²)	Number of HSU	CPU	System	Equipment name	Memory	Run time
4080	17547	Intel(R) Core i7	Windows 64-bit operating system	ThinkPad P15 Workstation	16G	<12min

5.2 Further Analysis of Prediction Performance

Using the 24-hour prediction results as an example, we randomly selected seven HSUs with false alarms for further analysis (Table 4). Columns 3–5 of Table 4 present the effective antecedent rainfall AER of these HSUs, the AER levels assigned by the database, and the relative errors, respectively. As shown in Column 5, the relative error ranges from 0.7% to 6.3%, indicating that the levels of the AER designed in the database can accurately reflect the effective antecedent rainfall characteristics of the HSUs. The average rainfall intensity, duration, and cumulative rainfall data at 24:00 are shown in Columns 6–8. As seen in Column 6, the cumulative rainfall for the seven HSUs ranges from 12 mm to 29.8 mm, with average rainfall intensities range from 0.5 mm/h to 1.25 mm/h, which can be classified as light to moderate rain type. The instability probability (HSU_{prob}) of these HSUs was calculated to investigate the causes of false positives. As shown in Column 9, among the seven HSUs with false alarms, five had an instability probability of less than 50%, indicating that



1 these HSUs did not experience instability during the rainfall process. Therefore, we cautiously
 2 conclude that although the prediction model exhibits preferable operational efficiency, it may
 3 increase the false-positive rate to some extent.

4 Table 4 The selected HSUs that report false alarms at 24:00

Numb er of HSUs	Slope gradient (°)	AER assignment			Daily accumulated rainfall (mm)	Duration (h)	Rainfall intensity I (mm/h)	HSU _{prob}
		Actual AER (mm)	AER levels assigned by the database (mm)	Relative error				
6172	19.4	74.6	70	6.2%	24.2	24	1.0	0.88
8561	26.5	70.9	70	1.3%	12.2	24	0.5	0.19
6066	26.7	83.1	80	3.7%	29.8	24	1.25	0.65
8535	25.9	68.6	70	2.0%	10.9	24	0.45	0.18
13108	40.3	74.1	70	5.5%	15.4	24	0.64	0.29
8297	23.4	70.5	70	0.7%	12.0	24	0.5	0.14
12966	38.3	74.7	70	6.3%	14.6	24	0.61	0.25

5 To investigate the potential for reducing the false-alarm rate, we selected four HSUs from Table
 6 4 for further analysis. Figures 10 a-d presented the I-D curves and cumulative precipitation
 7 distribution histograms for these HSUs.

8 For each HSU, the QPF data from 00:00 to 24:00 were discretized into 12 sets of rainfall
 9 intensity and duration data points at 2-hour intervals (represented by black and red solid dots). The
 10 black solid dots positioned below the I-D curve indicate that the HSU is stable at that moment,
 11 whereas the red solid dots located above the curve signify false alarms at the current forecasting
 12 hour. As shown in Figures 10a-d, the red false alarm points for the four HSUs are all situated very
 13 close to the I-D curve, nearly tangent to it. This proximity suggests that slight spatial adjustments
 14 to these points could alter the forecast results. Another important issue is that some of the black
 15 solid dots correspond to a cumulative rainfall of 0 mm, indicating that the rainfall process had not
 16 yet begun. Therefore, it is necessary to adjust the spatial positions of data points I and D based on
 17 the actual initiation time of the rainfall process, thereby facilitating an in-depth investigation of the
 18 causes of the false alarms.

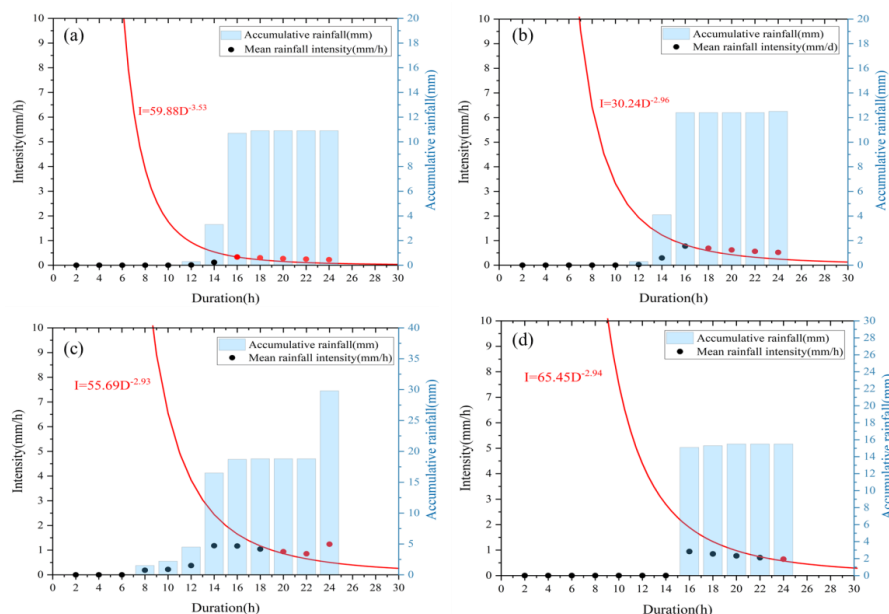


Figure 10 The I-D Curves of HSUs before the adjustment of rainfall process (a. 8535; b. 8561; c. 6066; d. 13108)

In this study, an HSU with number 8535 is taken as an example to illustrate the process of adjusting the spatial positions of data points I and D. As shown in Table 5, the rainfall process for this HSU started at 12:00 and ended at 24:00 with a duration of 12 h. The start time of rainfall was used as the starting point to recalculate the rainfall intensity during the rainfall process, as indicated in the text highlighted with a yellow background in Table 5. The adjusted average rainfall intensity was significantly higher than the values prior to adjustment. This means that the adjustment of the rainfall process led to notable changes in the spatial locations of the data points I and D. As shown in Figure 11a, after updating the positions of data points I and D, the HSU does not exhibit any false alarms. Figures 11b-d present the updated forecast results for the other three HSUs after the adjustment. As shown in Figure 11a-d, following the adjustments, three out of these four HSUs were able to release accurate results. Therefore, we advise that practical warning applications should consider the influence of the difference in rainfall processes of HSUs on the prediction results.

Table 5 Rainfall process adjustment for HSU with number of 8535

Time	2:00	4:00	6:00	8:00	10:00	12:00	14:00	16:00	18:00	20:00	22:00	24:00
Accumulated rainfall(mm)	0	0	0	0	0	0.3	3.3	10.7	10.9	10.9	10.9	10.9
Before adjustment	I(mm/h)	0	0	0	0	0	0.2	0.7	0.6	0.5	0.5	0.5



	D (h)	2	4	6	8	10	12	14	16	18	20	22	24
After adjustment	I(mm/h)	/					0	1.6	2.7	1.8	1.3	1.1	0.9
	D (h)	/					0	2	4	6	8	10	12

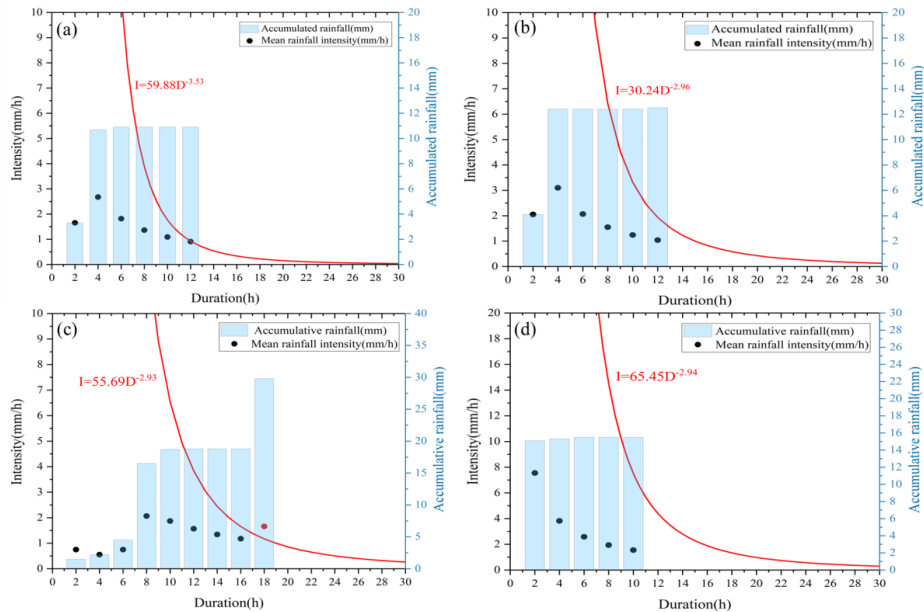


Figure 11 The I-D Curves of HSUs after the adjustment of rainfall process (a. 8535; b. 8561; c. 6066; d. 13108)

6 Conclusion

Currently, the operational forecasting of rainfall-induced landslides over regional scales of thousands of square kilometers faces significant challenges. Conventional physical and statistical approaches have shown limitations in terms of achieving satisfactory results. This study utilized HSU as a basis to integrate physical models and rainfall threshold methods for a warning model applicable to large-scale regions. The warning model employs HSU as a prediction unit to improve the clarity of the warning results, physical methods are utilized to develop the warning criteria, thereby reducing the overreliance on historical observational data, and a database of rainfall parameters across different rainfall scenarios is constructed, which enhances the efficiency and applicability of the warning model. The prediction performance was validated through a case study of “8.31” rainfall landslides in Fengjie County. The conclusions are as follows.



1 (1) A rainfall-triggered landslide warning model was established by integrating HSUs, physical
2 approaches, and rainfall parameters. Initially, a grid-based HSU hydrological analysis technique
3 was established to determine the soil moisture content distribution within the HSUs during different
4 rainfall hours. Subsequently, computer graphics algorithms, random search techniques, and
5 infinite slope models were used to develop a regional-scale HSU stability analysis method. Soil
6 mechanics parameters at the limit of water content and probability density functions were used to
7 describe the spatial uncertainty of the soil mechanical parameters within the HSU during rainfall
8 infiltration, allowing for the calculation of the instability probability of the HSU. Different rainfall
9 scenarios were simulated to derive rainfall intensity I and duration D data that can trigger HSU
10 instability, thereby constructing early warning curves for the rainfall thresholds of the HSU.

11 (2) A database for the I-D curve fitting parameters α and β across various AER levels was
12 established. This database includes α and β data for 17,547 HSUs across 20 AER levels, amounting
13 to a total of 350,940 records, thus offering substantial data support for rainfall-induced landslide
14 predictions in Fengjie County. In practical applications, it is sufficient to quickly issue warning
15 information by assessing the relationship between the values of I and αD^β , thereby reducing the time
16 required to calculate the safety factors using conventional physical models. The calculation
17 efficiency test indicates that the warning mode can perform forecasts for thousands of kilometers
18 within a runtime of less than 12 min, thereby meeting the operational needs for real-time warnings
19 over large regional scales.

20 (3) The case study indicates that the distribution trends of unstable HSUs align well with
21 rainfall characteristics. As the rainfall duration increased, the missing alarm rate (MAR) gradually
22 decreased, while the false alarm rate (FAR) continued to increase. Taking the 24-hour forecast
23 results as an example, the missing alarm rate was 11.8%, while the false alarm rate was 21.1%. ROC
24 analysis revealed that the accuracy of the forecast result at this moment was 80.7%, with a precision
25 of 79.1%, reflecting satisfactory overall forecasting performance. Further discussion of the false
26 alarm rate suggests that adjusting the spatial locations of rainfall intensity and duration data points
27 based on the rainfall characteristics of each HSU may be conducive to reducing false alarm rates.

28
29
30
31



1 Acknowledgements

2 The authors would like to acknowledge the Chongqing Meteorological Bureau, China for providing
 3 the QPE and QPF data free of charge. We are also thankful to the Land and Resources Bureau of
 4 Fengjie county for their support with the field investigation.

6 Conflict of Interest Statement

7 All authors declare that they have no conflicts of interest. We declare that we do not have any
 8 commercial or associative interests that represent a conflict of interest in connection with the
 9 submitted work.

11 Author contributions

12 **KW:** Conceptualization, Writing – original draft, Supervision, Data curation Funding acquisition;
 13 **LX:** Supervision, Visualization, Writing – original draft; **SX:** Investigation, Data curation,
 14 Validation; **SZ:** Methodology, Resources, Validation; **YJ:** Supervision, Validation, Software; **JZ:**
 15 Investigation, Software; **HG:** Investigation, Visualization; **LZ:** Project administration, Visualization;
 16 **ZW:** Project administration, Writing – review & editing; **FQ:** Writing – review & editing.

18 Disclosure statement

19 No potential conflict of interest was reported by the author(s).

21 Funding

22 This work was supported by the [National Natural Science Foundation of China] under Grant
 23 [42301083]; and [Key Scientific Research Project of Higher Education Institutions, Henan Province,
 24 China] under Grant [24A170033]; and [General Project of Henan Province Education Science
 25 Planning, China] under Grant [2025YB0116].

27 Data availability statement

28 The datasets supporting this study are available from the corresponding author upon reasonable
 29 request.

32 Reference

- 33 Alvioli, M., Guzzetti, F., & Marchesini, I. 2020. Parameter-free delineation of slope units and t
 34 errain subdivision of Italy. *Geomorphology*, 358, 107124. <https://doi.org/10.1016/j.geomorph.2020.107124>.
 35
 36 Aristizábal, E., Vélez, J. I., Martínez, H. E., & Jaboyedoff, M. 2016. SHIA_Landslide: a distri
 37 buted conceptual and physically based model to forecast the temporal and spatial occur
 38 rence of shallow landslides triggered by rainfall in tropical and mountainous basins. *La
 39 ndslides*, 13(3), 497-517. <https://doi.org/10.1007/s10346-015-0580-7>.
 40 Baum, R. L., Savage, W. Z., & Godt, J. 2008. TRIGRS—a Fortran program for transient rainf
 41 all infiltration and grid-based regional slope-stability analysis. US Geological Survey O
 42 pen File Report 2008-1159, 2.
 43 Bezak, N., Šraj, M., & Matjaž, M. 2016. Copula-based IDF curves and empirical rainfall thres
 44 holds for flash floods and rainfall-induced landslides. *Journal of Hydrology*, 541, 272-2



- 1 84. <https://doi.org/10.1016/j.jhydrol.2016.02.058>.
- 2 Bogaard, T., & Greco, R. 2018. Invited perspectives: Hydrological perspectives on precipitation
- 3 intensity-duration thresholds for landslide initiation: proposing hydro-meteorological thre
- 4 sholds. *Natural Hazards and Earth System Sciences*, 18, 31-39. [https://doi.org/10.5194/n](https://doi.org/10.5194/nhess-18-31-2018)
- 5 [hess-18-31-2018](https://doi.org/10.5194/nhess-18-31-2018).
- 6 Brunetti, M., Peruccacci, S., Rossi, M., S, L., Valigi, D., & Guzzetti, F. 2010. Rainfall threshol
- 7 ds for the possible occurrence of landslides in Italy. *Natural Hazards and Earth System*
- 8 *Sciences*, 10. <https://doi.org/10.5194/nhess-10-447-2010>.
- 9 Cuomo, S., Di Perna, A., & Martinelli, M. 2021. Modelling the spatio-temporal evolution of a
- 10 rainfall-induced retrogressive landslide in an unsaturated slope. *Engineering Geology*, 29
- 11 4, 106371. <https://doi.org/10.1016/j.enggeo.2021.106371>.
- 12 Domènech, G., Alvioli, M., & Corominas, J. 2019. Preparing first-time slope failures hazard m
- 13 aps: from pixel-based to slope unit-based. *Landslides*, 17, 249-265. [https://doi.org/10.10](https://doi.org/10.1007/s10346-019-01279-4)
- 14 [07/s10346-019-01279-4](https://doi.org/10.1007/s10346-019-01279-4).
- 15 Fawcett, T. 2006. Introduction to ROC analysis. *Pattern Recognition Letters*, 27, 861-874. [https:](https://doi.org/10.1016/j.patrec.2005.10.010)
- 16 [//doi.org/10.1016/j.patrec.2005.10.010](https://doi.org/10.1016/j.patrec.2005.10.010).
- 17 Greco, V. 1996. Efficient Monte Carlo Technique for Locating Critical Slip Surface. *Journal of*
- 18 *Geotechnical Engineering*, 122, 517-525. [https://doi.org/10.1061/\(ASCE\)0733-9410\(1996\)1](https://doi.org/10.1061/(ASCE)0733-9410(1996)122:7(517))
- 19 [22:7\(517\)](https://doi.org/10.1061/(ASCE)0733-9410(1996)122:7(517)).
- 20 Gu, T., Wang, J., Fu, X., & Liu, Y. 2014. GIS and limit equilibrium in the assessment of regi
- 21 onal slope stability and mapping of landslide susceptibility. *Bulletin of Engineering Ge*
- 22 *ology and the Environment*, 74, 1-11. <https://doi.org/10.1007/s10064-014-0689-2>.
- 23 Guo, Z., Torra, O., Hürlimann, M., Abancó, C., & Medina, V. 2022. FSLAM: A QGIS plugin
- 24 for fast regional susceptibility assessment of rainfall-induced landslides. *Environmental*
- 25 *Modelling & Software*, 150, 105354. <https://doi.org/10.1016/j.envsoft.2022.105354>.
- 26 He, X., Hong, Y., Vergara, H., Kirstetter, P.-E., Gourley, J., Zhang, Y., Qiao, G., & Liu, C. 20
- 27 16. Development of a Coupled Hydrological-geotechnical Framework for Rainfall-induc
- 28 ed Landslides Prediction. *Journal of Hydrology*, 543. [https://doi.org/10.1016/j.jhydrol.201](https://doi.org/10.1016/j.jhydrol.2016.10.016)
- 29 [6.10.016](https://doi.org/10.1016/j.jhydrol.2016.10.016).
- 30 Hong, M., Kim, J., & Jeong, S. 2017. Rainfall intensity-duration thresholds for landslide predic
- 31 tion in South Korea by considering the effects of antecedent rainfall. *Landslides*, 15. [h](https://doi.org/10.1007/s10346-017-0892-x)
- 32 [tps://doi.org/10.1007/s10346-017-0892-x](https://doi.org/10.1007/s10346-017-0892-x).
- 33 Hong, Y., Hiura, H., Shino, K., Sassa, K., Suemine, A., Fukuoka, H., & Wang, G. 2005. The
- 34 influence of intense rainfall on the activity of large-scale crystalline schist landslides in
- 35 Shikoku Island, Japan. *Landslides*, 2, 97-105. <https://doi.org/10.1007/s10346-004-0043-z>.
- 36 Huang, F., Tao, S., Chang, Z., Huang, J., Fan, X., Jiang, S.-H., & Li, W. 2021. Efficient and
- 37 automatic extraction of slope units based on multi-scale segmentation method for lands
- 38 lide assessments. *Landslides*, 18. <https://doi.org/10.1007/s10346-021-01756-9>.
- 39 Kanungo, D., & Sharma, S. 2014. Rainfall thresholds for prediction of shallow landslides arou
- 40 nd Chamoli-Joshimath region, Garhwal Himalayas, India. *Landslides*, 11, 629-638. [https:](https://doi.org/10.1007/s10346-013-0438-9)
- 41 [//doi.org/10.1007/s10346-013-0438-9](https://doi.org/10.1007/s10346-013-0438-9).
- 42 Kim, S., Chun, K., Kim, M., Catani, F., Choi, B., & Seo, J. I. 2020. Effect of antecedent rain
- 43 fall conditions and their variations on shallow landslide-triggering rainfall thresholds in
- 44 South Korea. *Landslides*, 18. <https://doi.org/10.1007/s10346-020-01505-4>.



- 1 Liang, W.-L., & Uchida, T. 2021. Performance and topographic preferences of dynamic and ste
- 2 ady models for shallow landslide prediction in a small catchment. *Landslides*, 19. [http](http://doi.org/10.1007/s10346-021-01771-w)
- 3 [s://doi.org/10.1007/s10346-021-01771-w](http://doi.org/10.1007/s10346-021-01771-w).
- 4 Ma, T., Changjiang, L., Lu, Z., & Bao, Q. 2015. Rainfall intensity–duration thresholds for the
- 5 initiation of landslides in Zhejiang Province, China. *Geomorphology*, 245. [https://doi.org](https://doi.org/10.1016/j.geomorph.2015.05.016)
- 6 [/10.1016/j.geomorph.2015.05.016](https://doi.org/10.1016/j.geomorph.2015.05.016).
- 7 Marra, F. 2018. Rainfall thresholds for landslide occurrence: systematic underestimation using c
- 8 oarse temporal resolution data. *Natural Hazards*, 95. [https://doi.org/10.1007/s11069-018-3](https://doi.org/10.1007/s11069-018-3508-4)
- 9 [508-4](https://doi.org/10.1007/s11069-018-3508-4).
- 10 Medina, V., Hürlimann, M., Guo, Z., Lloret, A., & Vaunat, J. 2021. Fast physically-based mod
- 11 el for rainfall-induced landslide susceptibility assessment at regional scale. *CATENA*, 2
- 12 01, 105213. <https://doi.org/10.1016/j.catena.2021.105213>.
- 13 Montgomery, D., & Dietrich, W. 1994. A Physically Based Model for the Topographic Control
- 14 on Shallow Landsliding. *Water Resources Research - WATER RESOUR RES*, 30, 1153
- 15 -1172. <https://doi.org/10.1029/93WR02979>.
- 16 Montrasio, L., & Valentino, R. 2016. Modelling Rainfall-induced Shallow Landslides at Differe
- 17 nt Scales Using SLIP - Part I. *Procedia Engineering*, 158, 476-481. [https://doi.org/10.10](https://doi.org/10.1016/j.proeng.2016.08.475)
- 18 [16/j.proeng.2016.08.475](https://doi.org/10.1016/j.proeng.2016.08.475).
- 19 Pinho, T., & Augusto Filho, O. 2022. Landslide susceptibility mapping using the infinite slope,
- 20 SHALSTAB, SINMAP, and TRIGRS models in Serra do Mar, Brazil. *Journal of Mou*
- 21 *ntain Science*, 19, 1018-1036. <https://doi.org/10.1007/s11629-021-7057-z>.
- 22 Pradhan, A., Lee, S.-R., & Kim, Y.-T. 2018. A shallow slide prediction model combining rainf
- 23 all threshold warnings and shallow slide susceptibility in Busan, Korea. *Landslides*. [htt](https://doi.org/10.1007/s10346-018-1112-z)
- 24 [ps://doi.org/10.1007/s10346-018-1112-z](https://doi.org/10.1007/s10346-018-1112-z).
- 25 Rigon, R., Bertoldi, G., & Over, T. 2006. GEOTop: A Distributed Hydrological Model with Co
- 26 upled Water and Energy Budgets. *Journal of Hydrometeorology*, 7, 2006. [https://doi.org/](https://doi.org/10.1175/JHM497.1)
- 27 [10.1175/JHM497.1](https://doi.org/10.1175/JHM497.1).
- 28 Rosi, A., Segoni, S., Canavesi, V., Monni, A., Gallucci, A., & Casagli, N. 2020. Definition of
- 29 3D rainfall thresholds to increase operative landslide early warning system performance
- 30 s. *Landslides*, 18. <https://doi.org/10.1007/s10346-020-01523-2>.
- 31 Rossi, G., Catani, F., Leoni, L., Segoni, S., & Tofani, V. 2013. HIRESSES: a physically based s
- 32 lope stability simulator for HPC applications. *Nat. Hazards Earth Syst. Sci.*, 13(1), 151
- 33 -166. <https://doi.org/10.5194/nhess-13-151-2013>.
- 34 Tarboton, D., & Goodwin, C. 1970. The SINMAP approach to terrain stability mapping.
- 35 Tufano, R., Formetta, G., Calcaterra, D., & De Vita, P. 2021. Hydrological control of soil thic
- 36 kness spatial variability on the initiation of rainfall-induced shallow landslides using a
- 37 three-dimensional model. *Landslides*, 18. <https://doi.org/10.1007/s10346-021-01681-x>.
- 38 Turel, M., & Frost, J. (2011). *Delineation of Slope Profiles from Digital Elevation Models for*
- 39 *Landslide Hazard Analysis*. [https://doi.org/10.1061/41183\(418\)87](https://doi.org/10.1061/41183(418)87)
- 40 Van Genuchten, M. 1980. A Closed-form Equation for Predicting the Hydraulic Conductivity of
- 41 Unsaturated Soils1. *Soil Science Society of America Journal*, 44. [https://doi.org/10.213](https://doi.org/10.2136/sssaj1980.03615995004400050002x)
- 42 [6/sssaj1980.03615995004400050002x](https://doi.org/10.2136/sssaj1980.03615995004400050002x).
- 43 Wang, K., Xie, S., Zhang, S., Zhu, L., Ma, J., Liu, D., & Yang, H. 2024. Creating a big data
- 44 source of landslide deformation stages: New thoughts on identifying displacement war



- 1 ning thresholds. *Journal of Asian Earth Sciences*, 266, 106120. <https://doi.org/10.1016/j.jseas.2024.106120>.
- 2
- 3 Wang, K., & Zhang, S. 2021. Rainfall-induced landslides assessment in the Fengjie County, Th
- 4 ree-Gorge reservoir area, China. *Natural Hazards*, 108, 1-28. <https://doi.org/10.1007/s11069-021-04691-z>.
- 5
- 6 Wang, K., Zhang, S., & Wei, F. 2019. Geotechnical mechanical parameters determination of pr
- 7 ediction unit based spatial interpolation technique. *JOURNAL OF NATURAL DISAS*
- 8 *TERS*, 28, 209-219. <https://doi.org/10.13577/j.jnd.2019.0523>.
- 9 Wang, K., Zhang, S., Xie, W.-l., & Guan, H. 2023. Prediction of the instability probability for
- 10 rainfall induced landslides: the effect of morphological differences in geomorphology w
- 11 ithin mapping units. *Journal of Mountain Science*, 20, 1249-1265. <https://doi.org/10.1007/s11629-022-7789-4>.
- 12
- 13 Wang, X., Zhang, L., Wang, S., & Lari, S. 2013. Regional landslide susceptibility zoning with
- 14 considering the aggregation of landslide points and the weights of factors. *Landslides*,
- 15 11. <https://doi.org/10.1007/s10346-013-0392-6>.
- 16 Yan, G., Cheng, H., Jiang, Z., Teng, L., Tang, M., Shi, T., Jiang, Y., Yang, G., & Zhou, Q. 2
- 17 021. Recognition of Fluvial Bank Erosion Along the Main Stream of the Yangtze Rive
- 18 r. *Engineering*, 19. <https://doi.org/10.1016/j.eng.2021.03.027>.
- 19 Zhang, S., Ma, Z., Li, Y., Hu, K., Zhang, Q., & Li, L. 2021. A grid-based physical model to
- 20 analyze the stability of slope unit. *Geomorphology*, 391, 107887. <https://doi.org/10.1016/j.geomorph.2021.107887>.
- 21
- 22 Zhang, S., Xu, C. X., Wei, F., Hu, K., Xu, H., Zhao, L. Q., & Zhang, G. P. 2019. A physics
- 23 -based model to derive rainfall intensity-duration threshold for debris flow. *Geomorphol*
- 24 *ogy*, 351, 106930. <https://doi.org/10.1016/j.geomorph.2019.106930>.
- 25 Zhang, S., Zhao, L., Delgado Tellez, R., & Bao, H. 2018. A physics-based probabilistic foreca
- 26 sting model for rainfall-induced shallow landslides at regional scale. *Natural Hazards a*
- 27 *nd Earth System Sciences*, 18, 969-982. <https://doi.org/10.5194/nhess-18-969-2018>.
- 28 Zhuang, J., Iqbal, J., Jianbing, P., & Tieming, L. 2014. Probability Prediction Model for Landsl
- 29 ide Occurrences in Xi'an, Shaanxi Province, China. *Journal of Mountain Science*, 11, 3
- 30 45-359. <https://doi.org/10.1007/s11629-013-2809-z>.
- 31 Zhuang, J., Peng, J., Xu, Y., Xu, Q., Zhu, X., & Li, W. E. I. 2016. Assessment and mapping
- 32 of slope stability based on slope units: A case study in Yan'an, China. *Journal of Eart*
- 33 *h System Science*, 125. <https://doi.org/10.1007/s12040-016-0741-7>.